A multi-functional biphasic water splitting catalyst tailored for integration with high performance semiconductor photoanodes

Jinhui Yang,[1,2] Jason K. Cooper,[1,2] Francesca M. Toma,[1,2] Karl A. Walczak, [1,2] Marco Favaro,[1,2] Jeffrey W. Beeman,[1,2] Lucas H. Hess, [1,2] Cheng Wang,[3] Chenhui Zhu,[3] Sheraz Gul,[4] Junko Yano,[1,4] Christian Kisielowski,[5,6] Adam Schwartzberg,[5,6] Ian D. Sharp[1,2,*]

[1]Joint Center for Artificial Photosynthesis, Lawrence Berkeley National Laboratory, Berkeley, CA 94720, United States

[2]Chemical Sciences Division, Lawrence Berkeley National Laboratory, Berkeley, CA 94720, United States

[3]Advanced Light Source, Lawrence Berkeley National Laboratory, Berkeley, CA 94720, United States

[4]Molecular Biophysics and Integrated Bioimaging, Lawrence Berkeley National Laboratory, Berkeley, CA 94720, United States

[5]Molecular Foundry, Lawrence Berkeley National Laboratory, 1 Cyclotron Road, Berkeley, CA 94720, USA

[6]Materials Sciences Division, Lawrence Berkeley National Laboratory, Berkeley, CA 94720, United States

[*] Corresponding author email: idsharp@lbl.gov

Abstract. Artificial photosystems are advanced by the development of conformal catalytic materials that promote desired chemical transformations, while also maintaining stability and minimizing parasitic light absorption for integration on surfaces of semiconductor light absorbers. Here, we demonstrate that multi-functional, nanoscale catalysts that enable high performance photoelectrochemical (PEC) energy conversion can be engineered by plasma-enhanced atomic layer deposition (PE-ALD). The collective properties of tailored $Co_3O_4/Co(OH)_2$ thin films simultaneously provide high activity for water splitting, permit efficient interfacial charge transport from semiconductor substrates, and enhance durability of chemically sensitive interfaces. These films comprise compact and continuous nanocrystalline Co_3O_4 spinel that is impervious to phase transformation and impermeable to ions, thereby providing effective protection of the underlying substrate. Moreover, a secondary phase of structurally disordered and chemically labile $Co(OH)_2$ is introduced to ensure a high concentration of catalytically active sites. Application of this coating to photovoltaic p^+n-Si junctions yields best-reported performance characteristics for crystalline Si photoanodes.

The capture of solar energy and its conversion to storable chemical fuel by photoelectrochemical (PEC) systems provides a promising route to overcoming the current global reliance on fossil fuels.[1,2] In such artificial photosynthetic systems, the oxidation of water or hydroxyl ions is a requirement for providing a sufficiently abundant source of protons and electrons for sustainably driving the fuel formation reaction. However, the oxygen evolution reaction (OER) presents significant challenges in catalysis and a kinetic bottleneck for solar fuels generation. Among OER catalysts, Co oxides (CoO_x) have been shown to possess desirable activity over a broad range of pH values.[3] Recent breakthroughs have provided insight into the nature of catalytically active sites at the atomic scale,[4-8] as well as the role of dynamic structural transformations from the resting to the active states.[9-11] Within this context, there has been considerable interest in the development of disordered or amorphous materials that exhibit enhanced catalytic activity relative to their crystalline counterparts.[12,13] However, associated mechanisms of enhanced activity are only beginning to emerge. For instance, it has been shown that cobalt phosphate undergoes progressive amorphization, which results in a transition from predominantly surface-confined catalysis on crystalline surfaces to volume-active catalysis in amorphous material.[10] Likewise, Bergmann and co-workers recently demonstrated that transformation to the active phase is accompanied by reversible amorphization of a sub-nm thick near-surface region of Co_3O_4 to $CoO_x(OH)_y$.[11] The proposed mechanisms present an intriguing picture of catalysis in dynamic materials, whereby increasing concentrations of catalytically active sites within the bulk can contribute to higher overall activity per geometric area. While mechanistic insights are important, achieving atomic level control of structure-function relationships is essential for creating high performance catalysts.

Despite the emerging benefits of disordered or amorphous systems for OER catalysis, interfacing these materials with semiconductor light absorbers remains an outstanding challenge. For example, disordered catalyst films tend to be hydrated and are subject to drying stress-induced cracking and delamination.[14,15] Such transformations introduce physical and chemical instabilities, particularly when the catalyst film is interfaced to a chemically sensitive semiconductor. In such cases, it is also necessary to form conformal coatings, while retaining optical transparency. Standard synthetic approaches for forming disordered catalysts, such as electrodeposition and other solution methods, are not well suited for achieving this combination of material properties. Here, we seek to translate catalyst design principles from solution-based synthesis approaches, in which chemically and structurally labile materials possess improved activity, to advanced vapor deposition methods capable of forming continuous and defined thin films compatible with semiconductor light absorbers. Drawing inspiration from recent studies that highlight the importance of volume transformation for increasing concentrations of OER

active sites, we use plasma-enhanced atomic layer deposition (PE-ALD) to create biphasic films comprising chemically and structurally labile $Co(OH)_2$ on top of compact nanocrystalline Co_3O_4 spinel layers. The presence of these two phases is important for simultaneously increasing catalytic activity and providing a stable interface to the substrate. Precise control of film thickness and conformality, afforded by PE-ALD, is crucial for creating closed films at the nanoscale, while also minimizing losses due to parasitic light absorption and eliminating traditional limitations associated with hydrated catalysts. Integration of biphasic $Co_3O_4/Co(OH)_2$ coatings with photovoltaic p^+n-Si junctions yields, to the best of our knowledge, the highest photoelectrochemical activity for OER reported to date on crystalline Si. We note that sub-monolayer mixed $Co_3O_4/Co(OH)_2$ films have been previously applied to Fe_2O_3, resulting in considerable catalytic activity improvements.[16] While such a coating is suitable for chemically robust light absorbers, such as hematite, it is not compatible with current high efficiency photoanode materials, which rapidly degrade under operational conditions. In the present work, biphasic CoO_x films with defined nanocrystalline interfaces and disordered surface layers were created by PE-ALD using exposure cycles of $CoCp_2$ and oxygen plasma at target temperatures ranging from 40 °C to 300 °C (see Methods section).[17,18] Deposition was initially performed onto the surfaces of p^+-Si (0.001-0.005 Ω/cm) and electrocatalytic (EC) activity for OER was evaluated under 1 M NaOH.

Electrochemical properties. As shown in Fig. 1a, electrocatalytic current density is significantly increased as the deposition temperature is decreased from 300 °C to 100 °C. The dependence of activity on deposition temperature can also be seen in Fig. 1b, which shows the current density at an applied electrochemical potential of 1.8 V vs. RHE, and Fig. 1c, which shows the overpotential (η) required to achieve current densities of 1 mA/cm^2 and 10 mA/cm^2. Maximum activity is observed at a deposition temperature of approximately 100 °C. However, further decrease of the deposition temperature to 40 °C leads to poor performance (Supplementary Fig. 1) due to incomplete precursor decomposition and incorporation of residual carbon into the thin film (Supplementary Fig. 2). To promote nucleation, deposition was intentionally performed onto the native silicon oxide,[19] which should act as a tunneling barrier and play an important role in defining interfacial charge transfer resistance. Nevertheless, we find improved PEC performance for PE-ALD of CoO_x onto the native oxide compared to HF etched surface (Supplementary Fig. 3). Furthermore, catalyst was also deposited onto tin-doped indium oxide (ITO), a transparent conducting oxide. As shown in Fig. 1d, we find that the catalytic activity of CoO_x/ITO is also higher at lower deposition temperature, indicating that the observed differences with deposition temperature are intrinsic features of the catalysts.

1 Capacitance measurements indicate that the electrochemically active surface areas per geometric

2 area do not vary as a function of deposition temperature (see Supplementary Fig. 4). Therefore,

3 we can conclude that changes of surface roughness are not responsible for the observed

4 differences in catalytic activity. As shown in Fig. 1e, atomic force microscopy (AFM) of the film

5 deposited at 100 °C reveals that the layer is planar and continuous, with a root mean square (rms)

6 roughness of 2.6 Å. We note that solid/liquid contact area can have a considerable impact on

7 apparent activity, with many of the highest activity catalysts characterized by large roughness

8 values.[20,21] Given the planar morphology of the PE-ALD catalyst studied here, the overpotentials

9 compare favorably with benchmarked CoO_x catalysts possessing much higher electrochemically

10 active surface area.[20,21]

11 **Atomic structure.** To identify the key properties that define catalytic function, we focus on

12 comparison of films deposited at 100 °C and 300 °C. To this end, we employed advanced low-

13 dose aberration-corrected electron microscopy, which enables characterization down to the level

14 of single atoms, while minimizing beam-sample interactions. Cross-sectional images of CoO_x

15 films deposited onto (100) p^+-Si at 100 °C and 300 °C reveal layer thicknesses of 3.2±0.2 nm

16 and 4.8±0.2 nm, respectively (Fig. 2a). For both cases, lattice fringes in the layers originate from

17 the nanocrystalline structure of the deposited material and their homogeneity across the films

18 indicates that grain diameters are comparable to the layer thicknesses.

19 To image individual grains, plan-view samples were prepared by PE-ALD onto Si_3N_4

20 membranes. Figure 2b&c show low dose rate (<300 $e^-/Å^2s$) images of pristine layers grown at

21 100 °C and 300 °C, respectively. Nanocrystalline grains are observed that form contiunous layers

22 and exhibit irregular shapes. The absence of moiré patterns suggests that a monolayer of

23 nanocrystals is imaged. Supplementary Figure 5 shows phase images at a higher magnification

24 and reveals that the films consist of nanocrystals with partly coherent interfaces and grain sizes

25 of 3.4±0.2 nm and 5.2±0.3 nm, respectively. Corresponding nano-diffraction patterns are

26 assigned to electron scattering from Co_3O_4 spinel,[22] in agreement with extended X-ray

27 absorption fine structure (EXAFS) measurements (Supplementary Fig. 6). Figure 2d(inset)

28 shows an analysis of the film texture of the sample grown at 100 °C, which is also characteristic

29 for films grown at 300 °C (Supplementary Fig. 7) and reveals no statistically significant

30 differences to account for the observed incease of catalytic activity at reduced deposition

31 temperature.

32 A striking difference observed between Fig. 2b,c is the existence of bright contrast features in the

33 grain boundaries of the sample deposited at 300 °C. Corresponding features are not observed

34 from the sample deposited at 100 °C, where we find that grains coalesce to form a dense film of

nanocrystalline Co_3O_4. These features exhibit the characteristic random pattern of an amorphous material next to crystal facets of the adjacent grains (Fig. 2d). The bright contrast suggests a lower mass density in these regions, which favours an assignment as pinhole defects associated with facet formation when the average grain size exceeds ~5 nm. These results suggest that formation of closed nanocrystalline layers is enabled by smaller and less strongly faceted grains grown at reduced temperature. At elevated deposition temperature, increased surface diffusion and more pronounced faceting may lead to formation of nanoscopic voids at grain boundaries.

While imaging of pristine grains was accomplished by limiting total doses to <300 $e^-/Å^2$, additional insight into the sensitivity of films to nanoscale void formation is achieved by exploiting beam-sample interactions to intentionally drive *in situ* atom diffusion and grain growth. As shown in Supplementary Fig. 8, along with the associated video, significant electron beam-induced grain coarsening of material deposited at 100 °C can be achieved by recording image series. Despite considerable atomic motion during such measurements, individual images give the appearance of a static grain structure,[23] allowing identification of the locations of all Co^{3+}, Co^{2+} and O^{2-} columns (Fig. 2e). Analysis of grain sizes in image series (Supplementary Fig. 8) reveals surface difusion-induced grain coarsening. Importantly, polycrystalline thin films remain void-free and compact in the presence of *in situ* beam-stimulated atom diffusion, grain coarsening, and grain reorientation when their average grain size is smaller than 4.5 nm. Films deposited at 300 °C exhibit a grain size of 5.2±0.3 nm and a tendency to create voids between facets of adjacent crystal grains.

Chemical properties. Angle-resolved X-ray photoelectron spectroscopy (XPS) reveals significant differences in the chemical composition of the surface as a function of deposition temperature (Fig. 3). All spectra are well described using reported parameters for Co_3O_4 and $Co(OH)_2$.[24] The sample deposited at 300 °C is dominantly composed of Co_3O_4, which comprises tetrahedral Co^{2+} and octahedral Co^{3+}. A small contribution from $Co(OH)_2$ is also observed and is likely due to a hydroxylated terminal surface. In contrast, the sample deposited at 100 °C is characterized by significant spectral contributions from both Co_3O_4 and $Co(OH)_2$. The components from $Co(OH)_2$ increase with increasing take-off angle, indicating that $Co(OH)_2$ is mainly present at the surface. This finding is consistent with X-ray absorption near edge structure (XANES) measurements, which homogeneously sample the films and reveal nearly identical overall composition of Co_3O_4 for material deposited at 100 °C and at 300 °C (Supplementary Fig. 9). While the $Co(OH)_2$ phase was not directly observed by TEM, this is not surprising considering that these hydroxide compounds often lack long-range crystalline order and have been described as oligomeric layered structures.[25] Together, the combination of results

from TEM, XPS, and XANES allows us to conclude that the bulk of both films is composed of Co_3O_4, whereas there is a surface layer of $Co(OH)_2$ atop the sample deposited at 100 °C. Such a difference in surface composition can have a dramatic effect on catalytic mechanisms, as discussed below.

Chemical transformation of Co_3O_4 surfaces to catalytically active $CoO(OH)$ or $CoO_x(OH)_y$ phases has been observed by *in situ* Raman spectroscopy and synchrotron X-ray spectroscopy, respectively.[11,26] However, electrochemical and gravimetric characterization of Co_3O_4 spinel has demonstrated bulk phase stability under OER conditions. Transformations to $CoO(OH)$ are restricted to the surface,[27] which has important implications for the present work. In particular, the phase stability of closed nanocrystalline films of Co_3O_4 is desirable for ensuring a durable interface with the substrate. However, phase stability also implies an upper bound for the concentration of active sites for planar, compact thin films of Co_3O_4 such as those formed at 300 °C. This limitation can be overcome by creation of biphasic $Co_3O_4/Co(OH)_2$ films at 100 °C. Unlike Co_3O_4, $Co(OH)_2$ possesses an open, layered structure that allows intercalation of water and ions from solution, as well as changes in Co oxidation state with minimal structural reorientation.[6,27,28] As such, $Co(OH)_2$ supports catalytic activity not just at its surface but also within its bulk volume. Therefore, the observation of $Co(OH)_2$ on material deposited at low temperature suggests that the catalytic activity is enhanced by the presence of a higher concentration of active sites.

It is known that active sites of solid state Co-based OER catalysis proceed through redox transitions of $Co^{3+} \rightarrow Co^{4+}$, with highest activity sites provided by the generation of two adjacent and electronically coupled Co^{4+} centers.[5,9,29] As shown in Fig. 4a, steady state polarization Tafel curves yield values of ~50 mV/dec and 70 mV/dec for films deposited at 100 °C and 300 °C on p^+-Si, respectively. These values are in the range of those previously reported for CoO_x under alkaline conditions,[12,25,27] and are consistent with fast electrochemical pre-equilibrium between Co^{3+}–OH and Co^{4+}–O , followed by the rate-limiting O–O bond formation step.[30-32] The lower Tafel slope from the 100 °C sample supports the hypothesis that the biphasic $Co_3O_4/Co(OH)_2$ promotes formation of active Co^{4+} sites. The deviations from linearity at higher current densities suggest a resistance to charge transport that is higher in the thicker film deposited at 300 °C.[12,32]

Cyclic voltammetry (CV) in the pre-OER potential range reveals that surface redox behaviour of Co^{2+} and Co^{3+} is correlated with catalytic activity.[6,12,25,27] As shown in Fig. 4b, for the case of material deposited at 100 °C, we observe two well-defined anodic peaks. These are denoted A_1 and A_2 and can be assigned to $Co^{2+} \rightarrow Co^{3+}$ and $Co^{3+} \rightarrow Co^{4+}$ oxidation reactions, respectively.[12,28] The similar areas of A_1 and A_2 is consistent with electrochemical transformation of Co^{2+} in the

as-deposited $Co(OH)_2$ phase to Co^{3+} in the form of $CoO(OH)$, followed by activation of Co^{4+}.[33] Fig. 4c shows a comparison of the first and second CV sweeps. Following the first cycle, there is a considerable reduction in the magnitude of A_1, whereas the magnitude of A_2 remains approximately constant. This is indicative of the known electrochemical behaviour of $Co(OH)_2$, in which the $Co^{2+} \rightarrow Co^{3+}$ reaction, which does not participate directly in the catalytic cycle but is associated with phase transformation to $CoO(OH)$,[30,31] is largely irreversible.[34]

Much weaker redox activity is observed in the pre-catalytic range for material deposited at 300 °C, which is consistent with surface site-confined catalysis on structurally robust Co_3O_4. In contrast, the larger areas of A_1 and A_2 on the 100 °C deposited material indicate that the biphasic $Co_3O_4/Co(OH)_2$ films contain higher concentrations of active sites. Thus, the biphasic coating creates a desirable balance of properties that are well suited for integration with chemically sensitive substrates; the phase stability of Co_3O_4 enables a durable substrate/catalyst interface, while facile chemical transformation of $Co(OH)_2$ promotes high catalytic activity.

Integrated photoanodes. We deposit the highly active $Co_3O_4/Co(OH)_2$ catalyst made by PE-ALD at 100 °C onto a p^+n-Si substrate to determine if electrocatalytic performance enhancements can be translated to PEC systems. As shown in Fig. 6a, these integrated photoanodes are characterized by a photocurrent density of 30.8 mA/cm^2 at 1.23 V vs. RHE and a saturation photocurrent density of ~37.5 mA/cm^2 under 1 Sun AM 1.5 simulated solar irradiation. This large saturation current is attributed to low parasitic light absorption losses enabled by the closed biphasic catalyst coating with a near optimal thickness for maximizing optocatalytic efficiency.[35] Comparison of the EC characteristics of CoO_x on p^+-Si to the PEC characteristics of analogous films deposited on p^+n-Si yields a photovoltage of 600 mV. Photovoltages generated from CoO_x films deposited at 100 °C and 300 °C are nearly identical.[17] Therefore, we conclude that the cathodic shift of onset potential obtained with the biphasic $Co_3O_4/Co(OH)_2$ catalyst is a consequence of improved catalytic activity. To the best of our knowledge, these *J-E* performance characteristics are the best reported to date for catalyst-coated crystalline Si photoanodes.[17,36-44] Importantly, catalysts that undergo chemical transformation from resting to active state are often characterized by high ion permeability and are susceptible to drying-induced cracking and delamination.[14,15] As shown in Supplementary Fig. 10, no change of performance is observed upon repeated cycling between PEC operation and drying. Chronoamperometric tests revealed the films to be functionally stable under illuminated operation for at least 72 h (Fig. 5b), with no evidence of Co loss to solution, as measured by inductively-coupled plasma mass spectroscopy (Supplementary Fig. 11). The multi-functional properties of our biphasic coating, in which the interfacial Co_3O_4 is chemically stable and a thin

and intimately contacted surface hydroxide provides high catalytic activity, represents an important advance for forming assemblies incorporating semiconductor light absorbers.

In summary, we have fabricated conformal, biphasic CoO_x catalysts that are engineered to provide high activity and compatibility with semiconductor photoelectrodes. The resulting films consist of conformal layers of spinel Co_3O_4 nanocrystals that coalesce to form partly coherent grain boundaries. The resistance of these Co_3O_4 spinel crystals to chemical transformation provides durable interfaces. At reduced deposition temperature, disordered surface layers of $Co(OH)_2$ are introduced that significantly improve electrocatalytic OER activity. This surface layer promotes chemical and structural transformation, thereby providing high concentrations of catalytically active sites. In contrast to traditional layered hydroxides, which are susceptible to drying-induced cracking and delamination, these biphasic films are simultaneously robust and active. Improved electrocatalytic activity translates to higher photoelectrochemical activity, as demonstrated by integration of the biphasic material onto the surface of p^+n-Si photoelectrodes, which represent the best reported for crystalline Si to date. These results demonstrate that PE-ALD is a powerful method for synthesizing multi-functional catalysts that support desired chemical transformations, permit efficient interfacial charge transport, and minimize parasitic light absorption due to their conformal nature even at very low thicknesses. Thus, partial decoupling of ALD surface reaction kinetics from thermal activation, enabled by plasma enhancement, provides opportunity to tailor novel materials and interfaces for achieving desired functionality.

Methods

Deposition of CoO_x by atomic layer deposition (ALD)

Plasma-enhanced ALD (PE-ALD) allows partial decoupling of surface oxidation kinetics from substrate temperature by introducing a source of highly reactive oxygen radicals to the system.[19,45] Therefore, substrate temperature can be used to affect thin film properties with reduced influence on ALD surface reaction kinetics. This is a powerful feature of PE-ALD and offers significant, yet underexplored, potential for tailoring of catalytic materials. Here, CoO_x catalyst films were deposited using a remote PE-ALD (Oxford FLexAl) process at substrate temperature ranging from 100 °C to 300 °C.[17,18] Cobalt precursor was $CoCp_2$ (98% Strem Chemicals) and oxygen plasma was the oxidant. The precursor lines, carrier gas lines, and the reactor walls were kept at 120 °C. The $CoCp_2$ precursor bubbler was heated up to 80 °C and bubbled with 200 sccm of high purity Ar gas during the precursor exposure half cycles. Oxygen gas flow was held constant at 60 sccm throughout the deposition process. The cobalt precursor exposure half cycle consisted of 5 s $CoCp_2$ dosing and 5 s purging. The remote oxygen plasma half cycle consisted of 1 s pre-plasma treatment, 5 s plasma exposure, and 15 s purging. The applied plasma power

1 was 300 W and was applied for 5 s during the oxygen plasma half cycle. The deposition chamber was

2 maintained at 15 mTorr at all times. Unless otherwise noted, 100 PE-ALD cycles were used for film

3 formation. This was selected based on evaluation of the electrochemical potential required to reach a

4 photocurrent density of 10 mA/cm^2 from p$^+$n-Si/CoO$_x$ electrodes as a function of the number of

5 deposition cycles (Supplementary Fig. 12), but future opportunity exists for optimization.

6 For characterization of CoO$_x$ films as electrocatalysts, deposition was performed onto highly doped p-Si

7 (p$^+$-Si, B-doped, 0.001-0.005 Ω cm^{-1}) and indium-doped tin oxide (ITO, 8-12 Ω cm^{-1}) following ultrasonic

8 solvent cleaning, followed by drying under flowing nitrogen. As described in the main text and shown in

9 Supplementary Fig. 3, we find that the electrocatalytic activities of samples made from CoO$_x$ deposited

10 onto the native oxide of Si exhibit superior performance relative to HF-treated Si. Therefore, unless

11 otherwise noted, all CoO$_x$/Si samples were deposited after cleaning but without etching the substrate in

12 HF.

13 <u>Formation of p$^+$n-Si junctions by ion implantation</u>

14 Starting substrates were single side polished Czochralski-grown n-type (P-doped) prime grade (100) Si

15 wafers with resistivity of 3.0 - 10 Ω cm. Ion implantation was employed for junction formation. Room

16 temperature implantation was performed at a 7° incident angle using ^{11}B accelerated to 45 keV with a

17 dose of 1×10^{14} cm^{-2} and 32 keV with a dose of 5×10^{14} cm^{-2}. In order to reduce contact resistance, the

18 backsides of the wafers were implanted with ^{31}P at 140 keV with a dose of 1×10^{14} cm^{-2} and 75 keV with a

19 dose of 5×10^{14} cm^{-2}. Dopant activation, both for the junction p$^+$ emitter layer and the n$^+$ back contact

20 layer, was achieved via rapid thermal annealing at 1000 °C for 15 s under flowing nitrogen.

21 <u>Photoelectrochemical testing</u>

22 For both electrochemical and photoelectrochemical (PEC) characterization, cyclic voltammetry (CV) was

23 performed using a Biologic potentiostat and a three electrode cell using a platinum wire as counter

24 electrode, a Hg/HgO (1 M NaOH) as reference electrode, and the CoO$_x$-coated sample as the working

25 electrode. Unless otherwise noted, CV data were collected at a scan rate of 100 mV/s. The Si working

26 electrodes were fabricated by scratching an indium-gallium eutectic (Aldrich) into the backside of the

27 wafer and affixing a copper wire using conductive silver epoxy (Circuit Works). Direct electrical contact

28 to ITO working electrodes was achieved using conductive silver epoxy (Circuit Works). The copper wire

29 was passed through a glass tube and the wafer was insulated and attached to the glass tube with Loctite

30 615 Hysol Epoxi-patch or 7460 adhesive. Electrodes were dried overnight before testing. The supporting

31 electrolyte was aqueous 1 M NaOH prepared using MilliQ water (18.2 MΩ·cm). All measurements were

32 performed using an air saturated solution. PEC CV tests were performed at 100 mW/cm^2 using a Solar

33 Light 16S-300-005 solar simulator equipped with an AM1.5 filter set and the sample was illuminated

1 through a quartz window of the cell. Steady state polarization Tafel analysis was performed after

2 correcting IR drop correction.

3 In order to determine if the surface roughness, and thus solid/liquid interfacial contact area, varies as a

4 function of deposition temperature, the double-layer capacitance was measured by collecting CVs as a

5 function of scan rate. The relative electrochemically active surface areas were calculated from the linear

6 slope of the scan rate dependent current density at the center point potential of the sweep. To eliminate

7 pseudocapacitance contributions, measurements were performed in an acetonitrile solution with 0.1 M

8 tetrabutylammoniumhexafluorophosphate as the electrolyte instead of the aqueous NaOH solution used

9 for the electrochemical activity measurements.

10 Chonoamperometric stability tests were performed under simulated AM1.5G radiation at 1 Sun using an

11 Oriel Sol3A. Samples were mounted into acrylic cells using compression-fit gaskets and electrolyte flow

12 was established using a peristaltic pump to prevent bubble accumulation on photoelectrode surfaces.

13 Measurements were performed at an applied electrochemical potential of 1.8 V *vs*. RHE in 1 M NaOH.

14 Aliquots of electrolyte were removed every ~24 h for ICP-MS analysis (see below).

15 Inductively coupled plasma mass spectrometry (ICP-MS)

16 ICP-MS was performed using an Agilent 7900 system run using He mode. The internal standard was Ge,

17 selected based on its 1st ionization potential and M/Z as compared to Co. The standard curve was

18 prepared from a stock solution of 10 ppm (Part #: 8500-6940, Agilent Technologies) at concentrations of

19 0.01, 0.1, 1, 10, and 100 ppb diluted in 1% HNO_3 prepared from 70% HNO_3 (>99.999% trace metals

20 basis, 225711, Aldrich) and Milli-Q water. Linear fitting of the calibration curve resulted in an R^2=1.000.

21 Sample solutions, collected at various times during the stability tests, were run as-is.

22 Atomic Force Microscopy (AFM)

23 AFM measurements were performed using a Bruker Dimension Icon system operated in Scanasyst mode

24 with Si tips (Bruker, Scanasyst – Air).

25 X-ray photoelectron spectroscopy (XPS)

26 XPS was performed using a monochromatized Al Kα source (hν = 1486.6 eV), operated at 150 W, on a

27 Kratos Axis Ultra DLD system at takeoff angles of 0° and 55° relative to the surface normal, and pass

28 energy for narrow scan spectra of 20 eV, corresponding to an instrument resolution of approximately 600

29 meV. Spectral fitting was done using Casa XPS analysis software. Spectral positions were corrected using

30 adventitious carbon by shifting the C 1s core level position to 284.8 eV and curves were fit with quasi-

31 Voigt lines following Shirley background subtraction. We note that the spectral components from cobalt

32 oxides overlap, making it difficult to distinguish between different oxides, though differentiation of Co^{2+}

1 from Co^{3+} is possible since the unpaired electrons from Co^{2+} result in a distinct satellite structure at higher

2 binding energies. In the present work, we constrained fitting to three parameters by using differential peak

3 positions, relative amplitudes, and approximate widths reported by Biesinger *et al.*[24]

4 X-ray absorption spectroscopy (XAS)

5 X-ray absorption spectra (XAS) were collected on beamline 7-3 at the Stanford Synchrotron Radiation

6 Lightsource (SSRL) with an average current of 500 mA and an electron energy of 3.0 GeV. The radiation

7 was monochromatized with a Si (220) double-crystal monochromator which was detuned to 50% of flux

8 maximum at Co K-edge. A N_2-filled ion chamber (I_0) was used to monitor the intensity of the incident X-

9 rays in front of the sample. XAS data were recorded as fluorescence excitation spectra using a 30-

10 element Ge solid-state detector (Canberra). The monochromator energy calibration was done with the first

11 peak maximum of the first derivative of Co foil spectrum (7709.5 eV). Powder reference samples were

12 diluted with boron nitride (~1% w/w) and then packed into 0.5 mm thick aluminum sample holders using

13 kapton film windows on both sides. Data reduction of the XAS spectra was performed using SamView

14 (SixPack software, Dr. Samuel M. Webb, SSRL). Athena software (IFEFFIT package)[46] was used to

15 subtract the pre-edge and post-edge contributions, and the results were normalized with respect to the

16 edge jump. A five-domain cubic spline was used for the background removal in k-space. The extracted k-

17 space data, $k^3\chi(k)$, was then Fourier transformed into real space (r-space) using a k-space window of 3.0-

18 11.30 Å^{-1}.

19 Transmission Electron Microscopy (TEM)

20 High resolution electron microscopy is known to be challenging since the probing electron beam can alter

21 the genuine structure before atomic resolution is reached. Minimization of beam-sample interactions is

22 particularly important for understanding the structures of low-temperature and potentially disordered thin

23 films, such as those investigated here. Recently, remarkable progress has been made in overcoming these

24 limitations by applying low dose rate in-line electron holography.[47,48] In this work, electron microscopy

25 was performed at the Molecular Foundry using microscopes operated at 300 kV. Images in Fig. 2a were

26 recorded with the One Angstrom Microscope.[49] All other experiments were performed with TEAM 0.5.[50]

27 The instrument allows control of beam-sample interactions by producing in-line holograms from image

28 series with variable dose-rates and by solving the phase problem.[48] The method builds on best practices

29 that were developed for the imaging of biological objects but uses large image series to obtain the needed

30 contrast in atomic resolution images. A resolution well below 1 Å is shown in Supplementary Fig. 5 that

31 allows for a reliable identification of crystal structures from real space images by indexing diffraction

32 spots using established crystal structures.[22] All reconstructions of exit wave functions and other

33 calculations were done with the McTempas software package (Kilaas).

In the low magnification mode, we recorded single images at a large underfocus, *f*, (Fig. 2b,c) where Fresnel fringes become prominent and differentiate the individual grains. As a result, specific spatial frequencies occur in the low spatial frequency spectrum of the Fourier Transform that characterize the average grain size, as shown in the insets of Fig. 2b,c. In high resolution images, individual grains are visible that we approximate by squares of area A^2. An average grain size, *A*, can be estimated by counting the number of grains, *N*, in a known field of view $B = N \times A^2$. Figure S8a summarizes these measurements for a recording of the same object with increasing dose rates, which allows the study of electron beam-induced grain growth and restructuring, as shown in Supplementary Fig. 8b,c, as well as the Supplementary Video.

Grain orientations were measured by taking a local Fourier Transform of individual grains from the reconstructed in-line holograms (i.e. complex electron exit wave functions), which are local nano-diffraction patterns (Fig. 2d) that cannot be obtained by direct diffraction work in broad beam mode. Texture analysis is limited by statistics since individual zone axis orientations can only be determined for grains that exhibit two independent sets of diffraction spots. Nevertheless, roughly 30% of the grains exhibit independent sets of diffraction spots that can be indexed to calculate zone axes orientations (Fig. 2d inset and Supplementary Fig. 7). The measured grain orientations cover most regions of the stereographic triangle of the cubic fcc single-crystal.

A standard cross-section sample preparation was performed using an Ar ion mill to thin samples consisting of CoO_x deposited on the native oxide of crystalline (100) Si substrates (Fig. 2a). For plane view observations, however, we deposited CoO_x directly onto an electron transparent silicon nitride membrane so that no additional sample preparation was necessary. Therefore, we can exclude any preparation-induced sample alteration that can occur during an exposure of small nanocrystals to the energetic beam of argon ions that is typically used for sample thinning. Depositions at both 100 °C and 300 °C yield continuous thin films that are composed of a monolayer of nanocrystalline material, which is determined by the absence of any Moire fringes.

Movie: The movie depicting crystal growth by surface diffusion and grain re-orientation was generated from the focus series marked by a circle in Figure 3. It consists of 60 images that were split into 6 series with 10 images, each, to reconstruct 6 wave functions. The phase of these six reconstructed electron exit wave function is shown as six images of a movie that lasts 0.5 seconds. Thus, a recording time of ~100 seconds is compressed into 0.5 seconds and the physical processes are shown accelerated by a factor of ~200× in time. The resolution in each image is maintained around 0.6Å, which enables a full separation of all Co and O atom columns in the [100] and [110] oriented grains that are imaged along their zone axes.

References

1   Tachibana, Y., Vayssieres, L. & Durrant, J. R. Artificial photosynthesis for solar water-splitting. *Nat Photon* **6**, 511-518 (2012).

2   Walter, M. G. *et al.* Solar Water Splitting Cells. *Chemical Reviews* **110**, 6446-6473, doi:10.1021/cr1002326 (2010).

3   Deng, X. & Tüysüz, H. Cobalt-Oxide-Based Materials as Water Oxidation Catalyst: Recent Progress and Challenges. *ACS Catalysis* **4**, 3701-3714, doi:10.1021/cs500713d (2014).

4   Friebel, D. *et al.* Identification of Highly Active Fe Sites in (Ni,Fe)OOH for Electrocatalytic Water Splitting. *Journal of the American Chemical Society* **137**, 1305-1313, doi:10.1021/ja511559d (2015).

5   Zhang, M., de Respinis, M. & Frei, H. Time-resolved observations of water oxidation intermediates on a cobalt oxide nanoparticle catalyst. *Nat Chem* **6**, 362-367, doi:10.1038/nchem.1874 (2014).

6   Burke, M. S., Kast, M. G., Trotochaud, L., Smith, A. M. & Boettcher, S. W. Cobalt–Iron (Oxy)hydroxide Oxygen Evolution Electrocatalysts: The Role of Structure and Composition on Activity, Stability, and Mechanism. *Journal of the American Chemical Society* **137**, 3638-3648, doi:10.1021/jacs.5b00281 (2015).

7   Sanchez Casalongue, H. G. *et al.* In Situ Observation of Surface Species on Iridium Oxide Nanoparticles during the Oxygen Evolution Reaction. *Angewandte Chemie International Edition* **53**, 7169-7172, doi:10.1002/anie.201402311 (2014).

8   Kanan, M. W. *et al.* Structure and Valency of a Cobalt−Phosphate Water Oxidation Catalyst Determined by in Situ X-ray Spectroscopy. *Journal of the American Chemical Society* **132**, 13692-13701, doi:10.1021/ja1023767 (2010).

9   Risch, M. *et al.* Water oxidation by amorphous cobalt-based oxides: in situ tracking of redox transitions and mode of catalysis. *Energy & Environmental Science* **8**, 661-674, doi:10.1039/C4EE03004D (2015).

10   González-Flores, D. *et al.* Heterogeneous Water Oxidation: Surface Activity versus Amorphization Activation in Cobalt Phosphate Catalysts. *Angewandte Chemie International Edition* **54**, 2472-2476, doi:10.1002/anie.201409333 (2015).

11   Bergmann, A. *et al.* Reversible amorphization and the catalytically active state of crystalline Co3O4 during oxygen evolution. *Nat Commun* **6**, doi:10.1038/ncomms9625 (2015).

12   Koza, J. A., He, Z., Miller, A. S. & Switzer, J. A. Electrodeposition of Crystalline Co3O4—A Catalyst for the Oxygen Evolution Reaction. *Chemistry of Materials* **24**, 3567-3573, doi:10.1021/cm3012205 (2012).

13   Indra, A. *et al.* Unification of Catalytic Water Oxidation and Oxygen Reduction Reactions: Amorphous Beat Crystalline Cobalt Iron Oxides. *Journal of the American Chemical Society* **136**, 17530-17536, doi:10.1021/ja509348t (2014).

14   Abdi, F. F. *et al.* Efficient solar water splitting by enhanced charge separation in a bismuth vanadate-silicon tandem photoelectrode. *Nat Commun* **4**, doi:10.1038/ncomms3195 (2013).

15   Sun, J., Zhong, D. K. & Gamelin, D. R. Composite photoanodes for photoelectrochemical solar water splitting. *Energy & Environmental Science* **3**, 1252-1261, doi:10.1039/C0EE00030B (2010).

16   Riha, S. C. *et al.* Atomic Layer Deposition of a Submonolayer Catalyst for the Enhanced Photoelectrochemical Performance of Water Oxidation with Hematite. *ACS Nano* **7**, 2396-2405, doi:10.1021/nn305639z (2013).

17   Yang, J. H. *et al.* Efficient and Sustained Photoelectrochemical Water Oxidation by Cobalt Oxide/Silicon Photoanodes with Nanotextured Interfaces. *Journal of the American Chemical Society* **136**, 6191-6194, doi:10.1021/ja501513t (2014).

18   Donders, M. E., Knoops, H. C. M., van, M. C. M., Kessels, W. M. M. & Notten, P. H. L. Remote Plasma Atomic Layer Deposition of Co3O4 Thin Films. *Journal of The Electrochemical Society* **158**, G92-G96, doi:10.1149/1.3552616 (2011).

19   George, S. M. Atomic Layer Deposition: An Overview. *Chemical Reviews* **110**, 111-131, doi:10.1021/cr900056b (2010).

20 McCrory, C. C. L., Jung, S. H., Peters, J. C. & Jaramillo, T. F. Benchmarking Heterogeneous Electrocatalysts for the Oxygen Evolution Reaction. *Journal of the American Chemical Society* **135**, 16977-16987, doi:10.1021/ja407115p (2013).

21 McCrory, C. C. L. *et al.* Benchmarking Hydrogen Evolving Reaction and Oxygen Evolving Reaction Electrocatalysts for Solar Water Splitting Devices. *Journal of the American Chemical Society* **137**, 4347-4357, doi:10.1021/ja510442p (2015).

22 Strada, G. N. M. Ossidi ed idrossidi del cobalto. *Gazzette Chimica Italiana* **58**, 419 (1928).

23 Alloyeau, D., Freitag, B., Dag, S., Wang, L. W. & Kisielowski, C. Atomic-resolution three-dimensional imaging of germanium self-interstitials near a surface: Aberration-corrected transmission electron microscopy. *Physical Review B* **80**, 014114 (2009).

24 Biesinger, M. C. *et al.* Resolving surface chemical states in XPS analysis of first row transition metals, oxides and hydroxides: Cr, Mn, Fe, Co and Ni. *Applied Surface Science* **257**, 2717-2730, doi:10.1016/j.apsusc.2010.10.051 (2011).

25 Gerken, J. B. *et al.* Electrochemical Water Oxidation with Cobalt-Based Electrocatalysts from pH 0–14: The Thermodynamic Basis for Catalyst Structure, Stability, and Activity. *Journal of the American Chemical Society* **133**, 14431-14442, doi:10.1021/ja205647m (2011).

26 Yeo, B. S. & Bell, A. T. Enhanced Activity of Gold-Supported Cobalt Oxide for the Electrochemical Evolution of Oxygen. *Journal of the American Chemical Society* **133**, 5587-5593, doi:10.1021/ja200559j (2011).

27 Trotochaud, L., Ranney, J. K., Williams, K. N. & Boettcher, S. W. Solution-Cast Metal Oxide Thin Film Electrocatalysts for Oxygen Evolution. *Journal of the American Chemical Society* **134**, 17253-17261, doi:10.1021/ja307507a (2012).

28 James B. Gerken, J. G. M., Jamie Y. C. Chen, Matthew L. Rigsby, William H. Casey, R. David Britt, and Shannon S. Stahl. Electrochemical Water Oxidation with Cobalt-Based Electrocatalysts from pH 0–14: The Thermodynamic Basis for Catalyst Structure, Stability, and Activity. *J. Am. Chem. Soc.* **133**, 12 (2011).

29 Plaisance, C. P. & van Santen, R. A. Structure Sensitivity of the Oxygen Evolution Reaction Catalyzed by Cobalt(II,III) Oxide. *Journal of the American Chemical Society* **137**, 14660-14672, doi:10.1021/jacs.5b07779 (2015).

30 Wang, H.-Y. *et al.* In Operando Identification of Geometrical-Site-Dependent Water Oxidation Activity of Spinel Co3O4. *Journal of the American Chemical Society* **138**, 36-39, doi:10.1021/jacs.5b10525 (2016).

31 Kim, W., McClure, B. A., Edri, E. & Frei, H. Coupling carbon dioxide reduction with water oxidation in nanoscale photocatalytic assemblies. *Chemical Society Reviews* **45**, 3221-3243, doi:10.1039/C6CS00062B (2016).

32 Surendranath, Y., Kanan, M. W. & Nocera, D. G. Mechanistic Studies of the Oxygen Evolution Reaction by a Cobalt-Phosphate Catalyst at Neutral pH. *Journal of the American Chemical Society* **132**, 16501-16509, doi:10.1021/ja106102b (2010).

33 Risch, M. *et al.* Water oxidation by amorphous cobalt-based oxides: in situ tracking of redox transitions and mode of catalysis. *Energy & Environmental Science* (2015).

34 Koza, J. A., Hull, C. M., Liu, Y.-C. & Switzer, J. A. Deposition of β-Co(OH)2 Films by Electrochemical Reduction of Tris(ethylenediamine)cobalt(III) in Alkaline Solution. *Chemistry of Materials* **25**, 1922-1926, doi:10.1021/cm400579k (2013).

35 Trotochaud, L., Mills, T. J. & Boettcher, S. W. An Optocatalytic Model for Semiconductor–Catalyst Water-Splitting Photoelectrodes Based on In Situ Optical Measurements on Operational Catalysts. *The Journal of Physical Chemistry Letters* **4**, 931-935, doi:10.1021/jz4002604 (2013).

36 Hill, J. C., Landers, A. T. & Switzer, J. A. An electrodeposited inhomogeneous metal-insulator-semiconductor junction for efficient photoelectrochemical water oxidation. *Nat Mater* **14**, 1150-1155, doi:10.1038/nmat4408 (2015).

37   Scheuermann, A. G. *et al.* Design principles for maximizing photovoltage in metal-oxide-protected water-splitting photoanodes. *Nat Mater* **15**, 99-105, doi:10.1038/nmat4451 (2016).

38   Chen, Y. W. *et al.* Atomic layer-deposited tunnel oxide stabilizes silicon photoanodes for water oxidation. *Nat Mater* **10**, 539-544 (2011).

39   Chen, L. *et al.* p-Type Transparent Conducting Oxide/n-Type Semiconductor Heterojunctions for Efficient and Stable Solar Water Oxidation. *Journal of the American Chemical Society* **137**, 9595-9603, doi:10.1021/jacs.5b03536 (2015).

40   Zhou, X. *et al.* 570 mV photovoltage, stabilized n-Si/CoOx heterojunction photoanodes fabricated using atomic layer deposition. *Energy & Environmental Science*, doi:10.1039/C5EE03655K (2016).

41   Mei, B. *et al.* Protection of p+-n-Si Photoanodes by Sputter-Deposited Ir/IrOx Thin Films. *The Journal of Physical Chemistry Letters* **5**, 1948-1952, doi:10.1021/jz500865g (2014).

42   Hu, S. *et al.* Amorphous TiO2 coatings stabilize Si, GaAs, and GaP photoanodes for efficient water oxidation. *Science* **344**, 1005-1009, doi:10.1126/science.1251428 (2014).

43   Sun, K. *et al.* Stable solar-driven oxidation of water by semiconducting photoanodes protected by transparent catalytic nickel oxide films. *Proceedings of the National Academy of Sciences* **112**, 3612-3617, doi:10.1073/pnas.1423034112 (2015).

44   Kenney, M. J. *et al.* High-Performance Silicon Photoanodes Passivated with Ultrathin Nickel Films for Water Oxidation. *Science* **342**, 836-840, doi:10.1126/science.1241327 (2013).

45   Profijt, H. B., Potts, S. E., van de Sanden, M. C. M. & Kessels, W. M. M. Plasma-Assisted Atomic Layer Deposition: Basics, Opportunities, and Challenges. *Journal of Vacuum Science & Technology A* **29**, 050801, doi:10.1116/1.3609974 (2011).

46   Ravel, B. & Newville, M. ATHENA, ARTEMIS, HEPHAESTUS: data analysis for X-ray absorption spectroscopy using IFEFFIT. *Journal of synchrotron radiation* **12**, 537-541 (2005).

47   Kisielowski, C. *et al.* Real-time sub-$\AA{}$ngstrom imaging of reversible and irreversible conformations in rhodium catalysts and graphene. *Physical Review B* **88**, 024305 (2013).

48   Kisielowski, C. *et al.* Instrumental requirements for the detection of electron beam-induced object excitations at the single atom level in high-resolution transmission electron microscopy. *Micron* **68**, 186-193, doi:10.1016/j.micron.2014.07.010 (2015).

49   Kisielowski, C. *et al.* Imaging columns of the light elements carbon, nitrogen and oxygen with sub Ångstrom resolution. *Ultramicroscopy* **89**, 243-263, doi:10.1016/S0304-3991(01)00090-0 (2001).

50   Kisielowski, C. *et al.* Detection of Single Atoms and Buried Defects in Three Dimensions by Aberration-Corrected Electron Microscope with 0.5-Å Information Limit. *Microscopy and Microanalysis* **14**, 469-477, doi:doi:10.1017/S1431927608080902 (2008).
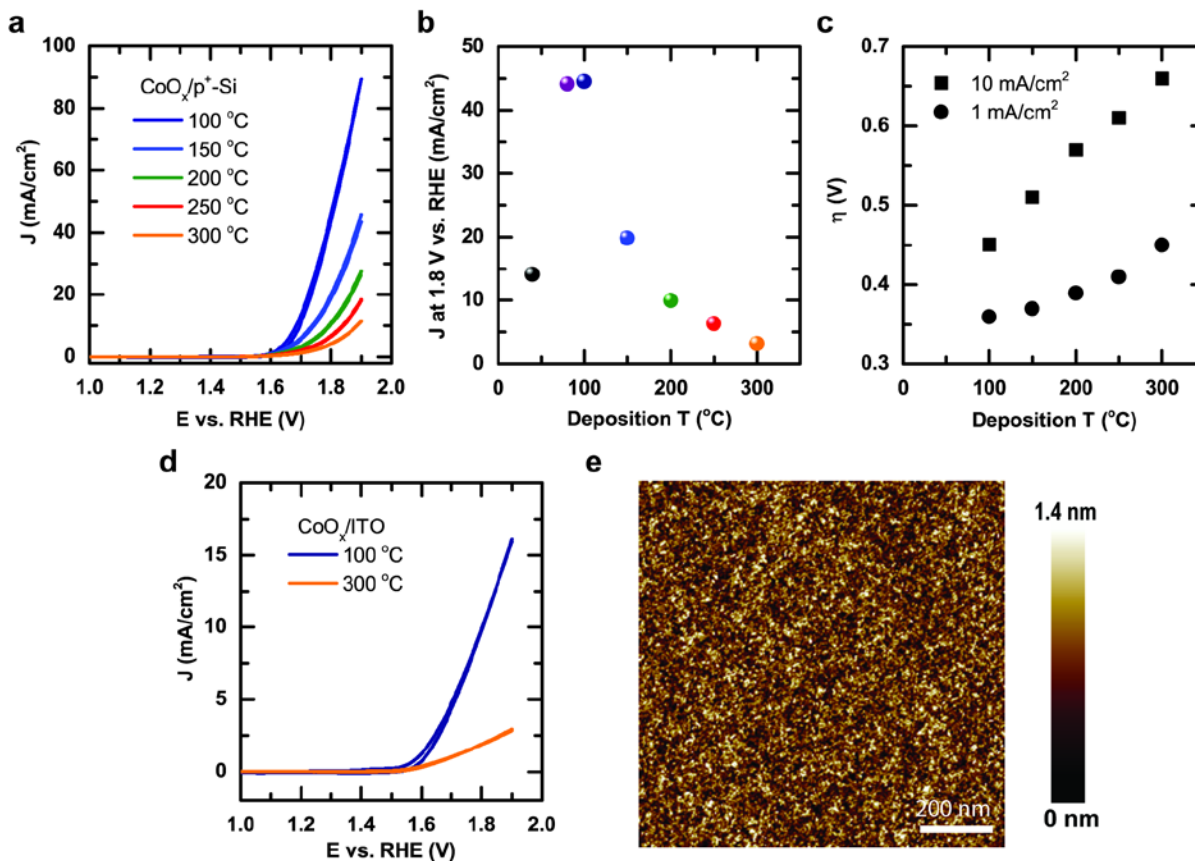
Acknowledgements

Author contributions

The manuscript was written through contributions of all authors. All authors have given approval to the final version of the manuscript.

Competing Financial Interests

The authors declare no competing financial interests.

1
2

Figures

3

Figure 1 | Electrocatalytic properties of CoO$_x$ films as a function of deposition temperature. a, Electrochemical current density versus applied electrochemical potential (*J-E*) curves as a function of growth temperature for plasma-enhanced atomic layer deposited CoO$_x$ thin films deposited on p$^+$-Si wafers. **b,** Electrochemical current density from the same films at a fixed potential of 1.8 V vs. RHE as a function of substrate temperature during deposition. **c,** Overpotential, η, required to achieve 10 mA/cm^2 (solid squares) and 1 mA/cm^2 (solid circles) as a function of deposition temperature. **d,** *J-E* curves from CoO$_x$ deposited onto tin-doped indium oxide (ITO) confirm that enhanced catalytic performance at reduced deposition temperature is an intrinsic feature of the films. **e,** Atomic force micrograph of a PE-ALD CoO$_x$ film grown at 100 °C on a (100) p$^+$-Si substrate, revealing an rms surface roughness of 2.6±0.2 Å. The corresponding measurement on material deposited at 300 °C yields an rms surface roughness of 2.8±0.8 Å. These findings, together with electrochemical capacitance measurements, indicate that observed differences of catalytic performance from these highly planar films are not due to surface roughness.

15

16
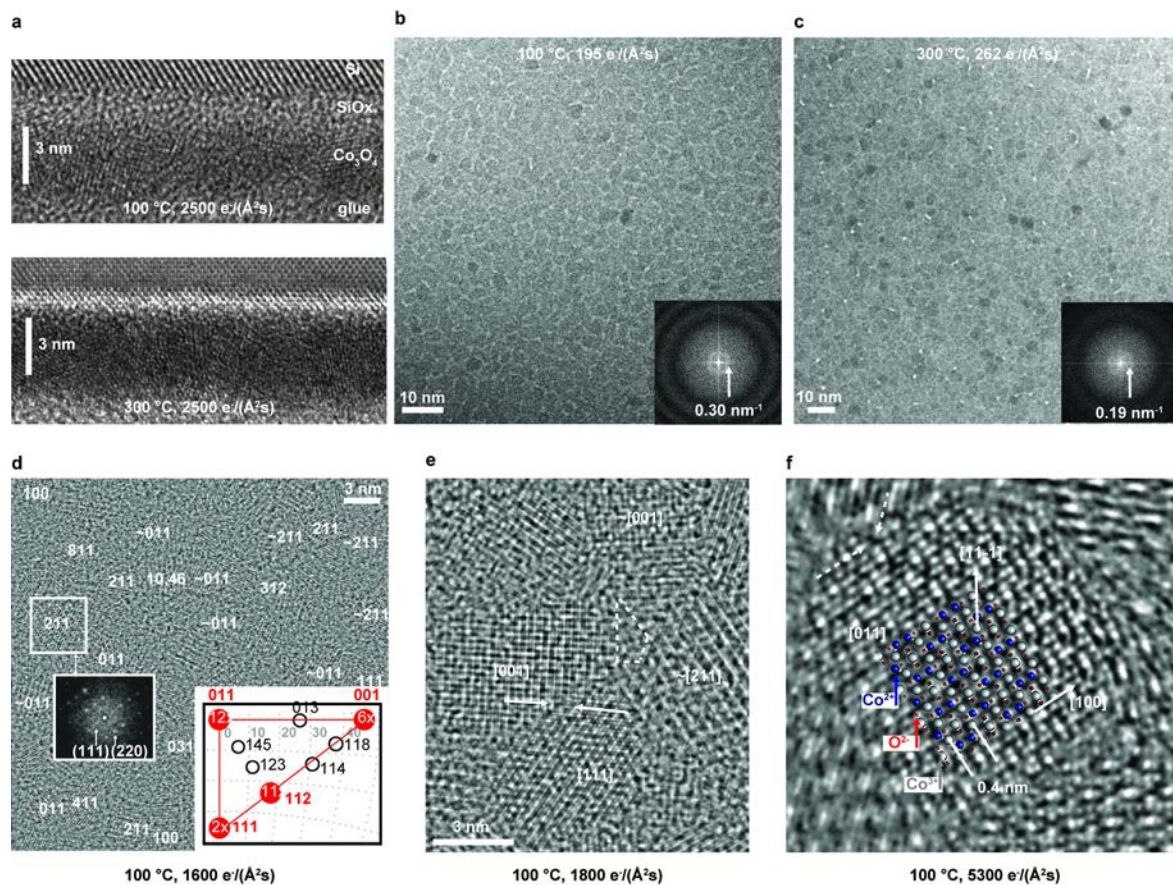
Figure 2 | Structural characterization of catalysts by transmission electron microscopy. a, Cross section micrographs of CoO$_x$ layers deposited at 100 °C (top) and 300 °C (bottom) on (100) Si, revealing thicknesses of 3.2±0.2 nm and 4.8±0.3 nm, respectively. A thin native silicon oxide layer is observed at the interface. **b,c** Low dose, plan view micrographs of films grown on amorphous Si$_3$N$_4$ membranes at: **b**, 100 °C and **c**, 300 °C. Dose rates are listed and single images were recorded with 1 s exposure. A large underfocus (**a**, f = -300 nm; **b**, f = -1000 nm) forces the appearance of Fresnel fringes that encircle individual grains and are evaluated in Fourier space (insets) to measure an average grain size of 3.3 nm in **a** and 5.3 nm in **b**. The different gray values of the grains are caused by electron scattering in crystalline material along variable zone axes orientations. Bright spots in **b** are dominantly located in boundaries between individual grains and suggest the presence of voids. **d**, Analysis of grain orientations for the 100 °C deposited sample is performed using the plan view phase image of the electron exit wave function, reconstructed from 50 images. The grains form partly coherent interfaces, with an average particle size of 3.4±0.2 nm. Approximately 30% of all grains exhibit two independent sets of reflection vectors that allow calculation of their zone axes, locally, as shown for a [211] grain and its nano-diffraction pattern (left inset). The corresponding stereographic triangle (right inset) of the cubic single-crystal highlights that a range of orientations were detected. **e,** Samples deposited at 300 °C are characterized by voids, as shown in the reconstructed phase

18

image, at high magnification (region bounded by dashed lines). The void shown here is bounded by crystal facets from adjacent [001], [211], and [111] oriented grains. **f**, The phase of the electron exit wave functions is reconstructed from a focus series of 50 images recorded on 100 °C deposited material using a high dose rate and accumulated electron dose of $9\times10^5\,e^-/\text{Å}^2$. A [011] oriented grain is shown, together with the projected crystal structure of Co_3O_4 spinel. Columns of Co^{3+}, Co^{2+}, and O^{2-}, can be readily distinguished. Grain boundaries are irregular and partly coherent (arrows) but void formation at interfaces is not observed, despite considerable beam-induced diffusion and coarsening. A movie depicting dynamic processes arising from beam-sample interactions is provided in the Supplemental Materials.
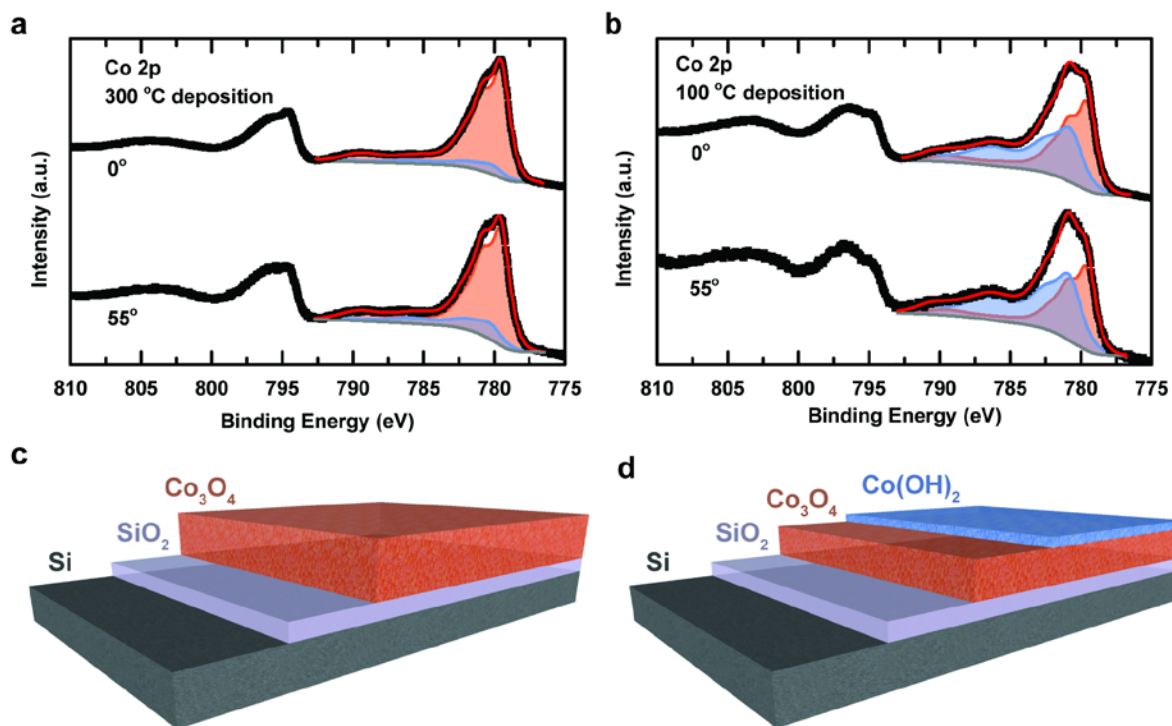
Figure 3 | Compositions and chemical states of tailored CoO$_x$ catalyst layers. Angle-resolved Co 2p X-ray photoelectron spectra acquired at 0° and 55° relative to the surface normal for CoO$_x$ films deposited on p$^+$-Si at: **a,** 300 °C and **b**, 100 °C. Constrained fitting of spectra reveals the presence of two phases, Co$_3$O$_4$ and Co(OH)$_2$, with their spectral contributions given by orange and blue, respectively. The relative intensity of the Co(OH)$_2$ component increases with increasing photoelectron takeoff angle, indicating that this material lies at the surface, as indicated in schematic illustrations of the films deposited at: **c**, 100 °C and **d**, 300 °C. Significant differences in phase composition are observed, with the biphasic character of material deposited at 100 °C allowing for considerably improved catalytic performance, as described in the text.
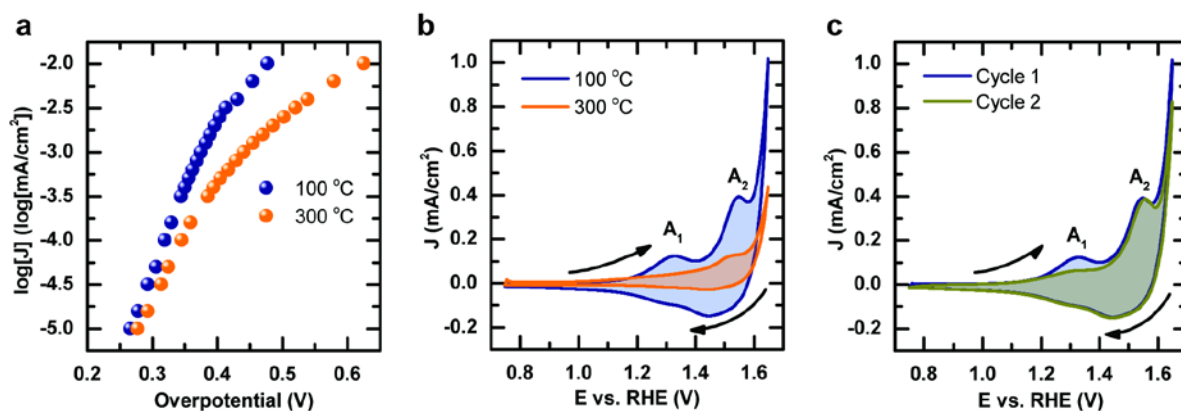
Figure 4 | Electrochemical characterization of chemical transformations of CoO_x catalysts. a, Steady-state Tafel plots measured in 1 M NaOH for CoO_x films deposited by PE-ALD on p^+-Si at 100 °C and 300 °C. The data were corrected for the IR drop in solution and yield Tafel slopes of 50 mV/decade and 70 mV/decade, respectively. **b,** Cyclic voltammograms (CVs) collected in the pre-OER catalytic region at 100 mV/s for samples deposited at 100 °C and 300 °C. Two oxidation peaks, labeled A_1 and A_2, are assigned to $Co^{2+} \rightarrow Co^{3+}$ and $Co^{3+} \rightarrow Co^{4+}$ reactions, respectively. The enhanced redox activity of the 100 °C material is due to the biphasic $Co_3O_4/Co(OH)_2$ film. **c,** Comparison of first and second CV scans from material deposited at 100 °C. The transformation of $Co(OH)_2$ to $CoO(OH)$ is largely irreversible, leading to a reduction in the A_1 peak after the first cycle. Activation of catalytically active Co^{4+} is unaffected by cycling, as exhibited by the approximately constant area of the A_2 oxidation peak.
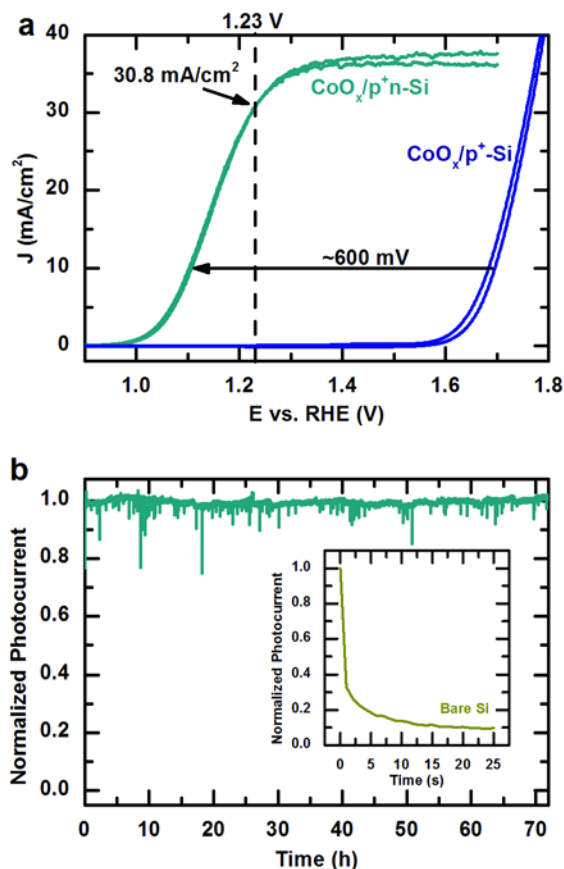
Figure 5 | Photoelectrochemical and stability characteristics of high performance CoO$_x$/Si photoanodes. a, Current density versus applied electrochemical potential (*J-E*) curves for biphasic Co$_3$O$_4$/Co(OH)$_2$ films deposited at 100 °C onto p$^+$-Si dark anodes and p$^+$n-Si photoanodes. A photovoltage of ~600 mV is obtained from the difference between these curves. The photoelectrodes exhibit the highest performance characteristics reported for crystalline Si to date, with an onset potential for water oxidation of < 1 V vs. RHE and a saturation current density of ~37.5 mA/cm^2. **b**, Normalized photocurrent as a function of time (*J-t*) reveals stable performance of p$^+$n-Si/Co$_3$O$_4$/Co(OH)$_2$ photoelectrodes for at least 72 h of continuous operation in 1 M NaOH under simulated 1 Sun illumination. By comparison, bare p$^+$n-Si photoelectrodes degrade nearly immediately (inset). Elemental analysis of the electrolyte during stability testing indicates no detectable transfer of Co from the film into solution (Supplementary Fig. 11), even after 72 h of operation.